# Coal-derived conductive pavement for winter de-icing: prototype, modeling, and simulation

Yawen He[1], Yucen Li[1], Yanhai Wang[1], Adam L. Brooks[1,2], Pawel Polaczyk[3], Baoshan Huang[1], and Hongyu Zhou[*,1]

[1]Department of Civil and Environmental Engineering, University of Tennessee, Knoxville, TN 39702, United States
[2]Nuclear Energy and Fuel Cycle Division, Oak Ridge National Laboratory, Oak Ridge, TN 37830, United States
[3]Department of Civil, Environmental, and Construction Engineering, Texas Tech University, Lubbock, TX 79409, United States

## Highlights

- A novel multifunctional pavement made from coal-derived solid carbon was developed.
- Mechanical, electrical, and thermal performance tests were performed.
- An efficient thermal network model was developed with experimental validation.
- Experiments and simulation studies demonstrated satisfactory de-icing performance.

## Abstract:

Existing pavement de-icing methods result in high installation and maintenance costs, traffic delays, excessive weariness and corrosion, and negative environmental and safety impacts. To overcome these challenges, this paper presents an innovative pathway to design and construct smart self-heating pavements using a low-cost coal-char bearing asphalt material. The conductive asphalt incorporates coal char, i.e., a key byproduct of the coal pyrolysis process, into the Stone Mastic Asphalt (SMA) mixture. This asphalt containing coal-derived solid carbon exhibits highly tailorable electrical conductivity, satisfactory mechanical and thermophysical properties, and superior cost-efficiency as

[*] Corresponding Author: Email: hzhou8@utk.edu, TEL: 01-865-974-0722, FAX: 01-865-974-2669; 851 Neyland Drive,417 John D. Tickle Building, Knoxville, TN 37996-2313, USA

compared to other conductive pavement materials. The de-icing performance was also demonstrated by laboratory experiments on a bench-scale prototype. Furthermore, an efficient thermal network model was developed and validated by experiments to investigate the transient thermal behavior and energy performance of the Ohmic heating pavement system. The whole-year energy simulation case studies were conducted on a bridge pavement with an annual energy use of 24.6 - 1444.8 kWh/$m^2$, showcasing its potential in field applications across cool humid, cold humid, and subarctic/arctic climate zones.

**Keywords:** *Self-heating pavement; Pavement de-icing; Conductive asphalt concrete; Electrical heating; Thermal network model; Multifunctional materials.*

| **Nomenclature** | |
|---|---|
| $A$ | Area [$m^2$] |
| $c_p$ | Specific heat [J/(K·kg)] |
| $F$ | View factor [–] |
| $G_{mb}$ | Bulk specific gravity of the compacted sample [–] |
| $G_{sb}$ | Aggregate bulk specific gravity [–] |
| $H$ | Heat transfer coefficient [W/K] |
| $I_s^{\downarrow}$ | Solar radiation incident [$W/m^2$] |
| $J_c$ | Critical strain energy release rate (J-integral) [$kJ/m^2$] |
| $L_{pre}$ | Precipitation [mm] |
| $m$ | Mass [kg] |
| $q$ | Heat rate [$W/m^3$] |
| $Q$ | Heat rate [W] |
| $R_E$ | Electrical resistance [Ω] |
| $t$ | Time [s] |
| $T$ | Temperature [K] |
| $V$ | Differential control volume or finite control volume [$m^3$] |
| *Greek symbols* | |
| $\alpha$ | Solar absorptance [–] |
| $\varepsilon$ | Surface emissivity [–] |
| $\zeta$ | Electrical resistivity [Ω·m] |
| $\lambda$ | Thermal conductivity [W/(m·K)] |
| $\rho$ | Density [$kg/m^3$] |
| $\sigma$ | Stephan-Boltzmann constant [$W/(m^2 \cdot K^4)$] |
| *Subscripts and superscripts* | |
| *abs* | Thermodynamic temperature |
| *air_ex* | Outdoor air or ambient air |
| *el* | Electric heating |
| *grd* | Ground (long-wave radiation) |
| *lw* | Long-wave radiation |
| *sky* | Sky (long-wave radiation) |
| *sw* | Short-wave radiation |

## 1. Introduction

Cold weather events lead to slippery road conditions due to the accumulation of ice and snow, which significantly undermine public safety, traffic efficiency, and travel experience. Car crashes induced by snow or sleet on roadways accounted for 31% of total

weather-related crashes [1] from 2007 to 2016 according to the 10-year statistics summary from the U.S. Federal Highway Administration (FHWA). The consequential traffic congestion or disruptions and human injuries [2] result in substantial economic losses [3]. To tackle these challenges, various techniques have been explored for roadway de-icing systems. To date, there are mainly three strategies to remove the snow or ice on pavements [4] – i.e., the mechanical methods (e.g. snow shoveling and plowing), the chemical methods (e.g. abrasives and chloride-based de-icing salts), and thermal techniques (e.g. electric or geothermal heating systems). While effective, mechanical methods also entail high maintenance costs, traffic delays, and weariness to road surfaces [5]. Deicers and chemical agents can incur soil contamination, pollution into ground and surface water, and corrosion to the pavements and vehicles, which deteriorates the ambient environment and increases safety risks [4]. Moreover, the expensive traditional de-icing techniques for winter road maintenance consume approximately 20 percent of state Departments of Transportation (DOT) maintenance budgets [6].

To overcome these limitations, different types of heated pavement systems such as geothermal heat pipes [4] and electrical coils [6] were studied as alternative methods for pavement de-icing [7]. In spite of the improvements in snow removal, traffic efficiency, and environmental benefits, these pavement de-icing systems [8] entail high installation, operation, and maintenance costs. To this end, prior studies mainly investigated the feasibility of transforming pavement materials into electrically conductive composites such as conductive asphalt or concrete [9,10] to serve as a heating layer within the pavement structure. Electrically conductive additives (i.e., conductive fibers, powders, or solid particles) were added to the concrete or asphalt to increase the

electrical conductivity and functionalize the material as an Ohmic heating element [11]. Recent studies have demonstrated the superior economic viability of conductive concrete [12] and conductive hot mix asphalt [10] with lower installation and maintenance costs than other de-icing systems [13] such as heating coils or pipes [14]. Despite the aforementioned advantages provided by existing conductive pavement de-icing systems, several limitations impede their widespread applications. The high initial cost and susceptibility to cracking and warping confined the applications of conductive concrete pavement in airfields, parking lots, and driveways [15]. Additionally, most electrically conductive additives in prior explorations such as carbon fiber, carbon black, graphite, and graphene are costly [16–19] for scale-up implementations. Furthermore, percolated network formulation in conductive pavements requires a high volume fraction of specific additives (e.g., 30 vol% for carbon black [20]). These add difficulties to securing the cost efficiency of conductive pavements. On the other hand, fibrous additives such as carbon fiber cause significant changes in the rheological properties of asphalt mixtures, making them difficult to compact [21]. The increased construction complexity has largely constrained its field implementation [22].

To address these challenges faced by existing conductive pavement technology, this paper proposed an innovative pathway to design and construct a smart pavement that transcends roadways to multifunctional systems capable of self-sensing and self-heating for de-icing. The coal-derived solid carbon, a key byproduct of the coal pyrolysis process, was employed to develop a low-cost coal-char bearing multifunctional material. Due to its mechanical, electrical, and thermal properties, coal char particles within the asphalt system not only serve as load-bearing fillers but also enable electric heating of the

pavement structure. The percolated coal-char aggregate network within the pavement material enhances its electrical conductivity [23] and enables Ohmic heating for road surface de-icing. Moreover, the piezoresistive behavior arising from the unique carbon-bitumen microstructure can be leveraged for continuous self-sensing of the pavement condition [24]. Replacing traditional aggregates with coal char maintains satisfactory mechanical performance and workability of the conductive asphalt mixture. This allows the same paving equipment and process as regular pavement constructions without extra costs while enhancing traffic flow, corrosion protection, and public safety. Furthermore, coal-derived carbon with a price of $200/ton is substantially more economical than other conductive additives considered for conductive pavements e.g., carbon fiber at $32,000/ton, and carbon black at $1,960/ton. This innovative integration of domestic coal resources into value-added infrastructure materials for bridge and road construction pipelines not only reduces direct usage as fuel but also yields environmental and economic benefits.

This paper presents the prototype, modeling, and control of the multifunctional pavement made from coal-derived carbon for winter de-icing. Key contributions and innovations of this work include:

1) The design and manufacturing process of coal char-charged asphalt mixture were illustrated. Multi-scale material tests were performed to characterize the mechanical, electrical, and thermophysical properties of conductive asphalt containing coal-derived solid carbon following standard tests [23,25,26].
2) A laboratory prototype was designed and produced. A bench-scale slab heating and de-icing experiments were conducted to study the thermal

behavior in different scenarios and demonstrate the de-icing capability of the coal char-charged conductive asphalt pavement system using Ohmic heating.

3) A thermal network model was developed for transient thermal behavior simulation of the conductive self-heating pavement. The model demonstrated satisfactory accuracy through experimental validation while maintaining high computational efficiency [27].
4) To assess the field performance of the coal-derived smart pavement, simulation case studies were performed on bridge pavements in multiple representative climate zones. The calibrated thermal network model was used for whole-year transient heat transfer and energy analyses. The thermal performance and energy consumption of the heating pavement were evaluated.

## 2. Materials – coal-char bearing conductive asphalt mixture

### 2.1. Material preparation

In this study, an electrically conductive coal-char bearing Stone Mastic Asphalt (SMA) mixture was developed as a multifunctional pavement de-icing system. This pavement assembly features a coal-derived conductive SMA layer sandwiched between a surface course and a base course developed from non-conductive dense-graded hot mix asphalt (HMA) mixtures. The asphalt mixture was designed and optimized for each of these three courses based on standard specifications for road and bridge construction, including those from the Tennessee Department of Transportation (TDOT) [28], the design and constructing standard for SMA mixtures by National Asphalt Pavement Association (NAPA) [29] and Superpave mix design manual [30]. The surface course

was constructed using a "411-D" mixture denoted by TDOT [28], while the base course used a TDOT "BM2" mixture [28]. The electrically conductive coal-char bearing SMA mixture consists of the asphalt binder, limestone, and coal-char aggregate. Given that the specific gravity of coal-char aggregate is lower than that of limestone aggregate, the asphalt mixture was designed by volume proportion.

The aggregate gradation curves by volume proportion for these three mixtures are presented in Figure 1. The coal char with particle size mainly ranging from 2.36 - 4.75 mm was utilized to develop an electrically conductive skeleton of the SMA mixture. The coal char particles smaller than 2.36 mm were employed as fine aggregates for conductive SMA mixture, where the coal char powders passing #200 sieve (<75μm) were obtained through grinding the as-received coal char aggregate using a ball mill. The coarse aggregates for the conductive SMA mixture, defined as those ranging from 2.36 mm to 9.5 mm, comprise a blend of coarse limestone aggregate and coarse coal char aggregate (60 wt% coal char of total aggregate weight and 40 wt% of limestone). The aggregate properties including specific gravity and absorption for the three mixtures are presented in Table 1.

Table 1 Constituent material properties of the aggregates

| Material Mixture | Aggregate | | $G_{sb}$ [—] | Absorption [%] |
|---|---|---|---|---|
| Surface course | Coarse (4.75 - 15.9 mm) | Limestone | 2.714 | 1.0 |
| | Fine (0 - 4.75 mm) | | 2.722 | 0.9 |
| Conductive SMA mixture | Coarse (2.36 - 9.5 mm) | Limestone | 2.716 | 1.4 |
| | | Coal char | 1.061 | 20.1 |
| | Fine (0 - 2.36 mm) | Limestone | N.A. | N.A. |
| | | Coal char | 1.264 | 16.2 |
| Base course | Coarse (4.75 - 31.8 mm) | Limestone | 2.724 | 0.9 |
| | Fine (0 - 4.75 mm) | | 2.736 | 0.7 |

The SBS-modified PG 76-22 asphalt binder was used for the conductive SMA mixture and PG 64-22 was used in the surface course and base course mixtures, with their properties enlisted in Table 2. The mixture's composition was adjusted to reach a desired air void content of 4%. The design weight (volume) proportions of asphalt binder, coal char, and limestone aggregate for the conductive SMA mixture are 18.7 wt% (23.8 vol %), 48.9 wt% (56.6 vol%), and 32.4 wt% (15.6 vol%), respectively. The optimum asphalt content, air void, voids in mineral aggregates (VMA), and voids filled with asphalt (VFA) of asphalt mixtures for each course are presented in Table 3 [29]. The optimum asphalt content and VMA of the conductive SMA mixture are 18.7% and 17.8%, which are compliant with the recommended lower limits of 6.0% and 17.0% [29], respectively.

Table 2 Properties of the asphalt binder

| Asphalt type | Viscosity at 135 °C [Pa·s] | Flash point [°C] | Specific gravity [60/60°F] | Polymer content [%] | Mixing temperature [°C] | Compaction temperature [°C] |
|---|---|---|---|---|---|---|
| PG 76-22 | 1.35 | 326 | 1.029 | 3.40 | 180 | 170 |
| PG 64-22 | 0.5 | 298 | 1.013 | 0 | 155 | 144 |

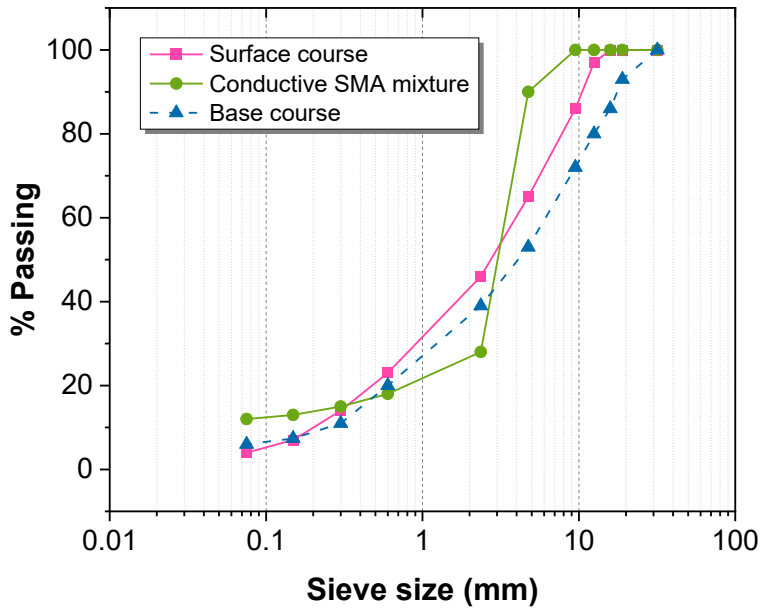


Figure 1 Aggregate gradation curve of the three asphalt mixtures

Table 3 Properties of the asphalt mixtures

| Material Mixture | Optimum asphalt content [%] | $G_{mb}$ [–] | Air Void [%] | VMA [%] | VFA [%] |
|---|---|---|---|---|---|
| Surface course | 5.4 | 2.437 | 4.0 | 15.2 | 73.7 |
| Conductive SMA mixture | 18.7 | 1.492 | 4.0 | 17.8 | 77.5 |
| Base course | 4.8 | 2.478 | 4.0 | 13.1 | 69.5 |

### 2.2. Microstructure

To study how coal-derived SMA compositions influence the material behavior from the microscale to the macroscale, the microstructure of the conductive SMA mixture made for this study was analyzed. A high-resolution 3D X-ray Micro Computed-Tomography (Micro-CT) system (*Skyscan* 1275) was used to provide data for non-destructive 3D model reconstruction. Cylindrical samples with the same dimension of 25 mm in height and 25 mm in diameter were scanned with an isotropic voxel size of 9 μm. The Micro-CT system conducted repeated scans of the sample through 360° rotation by a small increment (0.2° - 0.4°) to generate the three-dimensional micrography data. Its numerical counterparts were stored as a set of pixel matrices. The microstructure of the coal-char bearing SMA mixture sample is presented in Figure 2 by 3D reconstruction in ORS Dragonfly using the micro-CT data.

As shown in Figure 2, the conductive SMA mixture is composed of limestone, Stone Mastic Asphalt, and coal char, which are highlighted in yellow, black, and grey color, respectively. The reconstructed 3D microstructure model indicates that the limestone comprising less than 15 % of this mixture sample by volume, forms contact force chains within the material contributing to partial load bearing [31]. The coal char particles marked in the grey area, form a percolated network throughout the material. This creates a highly electrically conductive pathway that enables the entire SMA

mixture to act as an Ohmic heating element. The asphalt denoted by the black area serves as the matrix that binds all the granular particles together to form the pavement structure. It is noted that the coal char constitutes over 50% of the conductive SMA mixture by volume. In this configuration, sufficient coal char particles form the fundamental skeleton to function as the primary electrically conductive network for electric heating and contact force chains for load bearing [32]. Consequently, the mechanical and electrical properties of this composite material are predominantly governed by the interaction among coal char particles. Further discussions on alternative ways to design coal-char bearing conducive asphalt mixture for enhanced mechanical properties can be found in the authors' other publications.

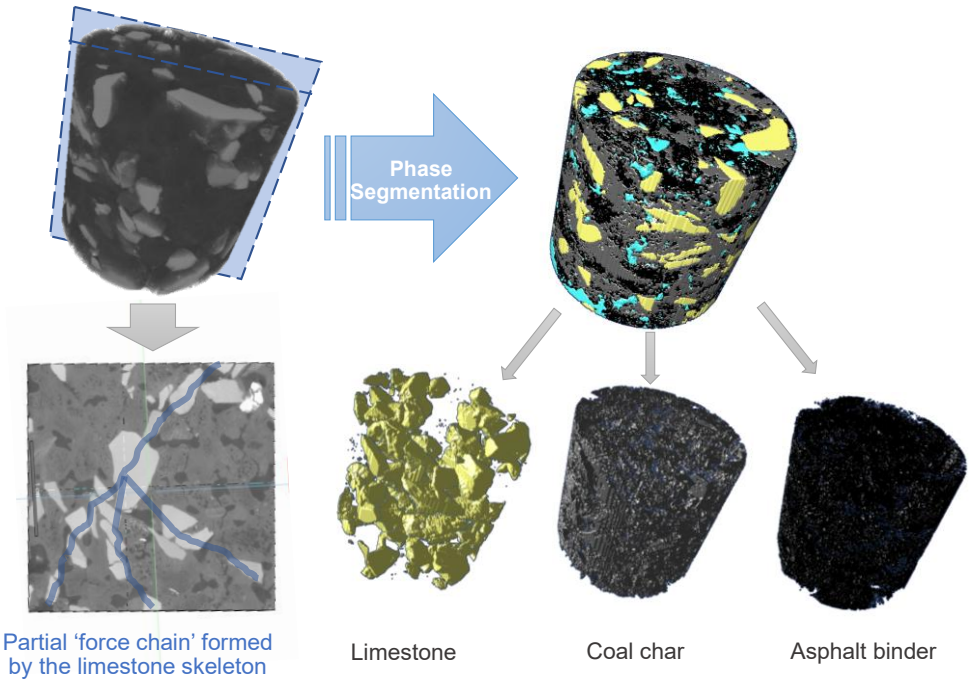


Figure 2 Microstructure of coal-char bearing conductive SMA mixture by 3D reconstruction using micro-CT data.

## 2.3. Properties of the conductive asphalt

### *2.3.1. Mechanical properties*

The mechanical performance of the coal-char bearing conductive asphalt mixture was evaluated by a series of material tests illustrated in Figure 3 (a) - (e). The shear strength of the mixture was measured using a direct shear test apparatus at a loading rate of 50 mm/min [33]. The rutting susceptibility/rutting resistance was assessed by rutting depth using an asphalt pavement analyzer (APA) following AASHTO T 340 [25]. In this test, the specimens were subjected to a contact pressure of 690 ± 35 kPa under 8,000 loading cycles to determine the rutting depths. The material stiffness was gauged by the resilient modulus under cyclic loading, which induces horizontal deformation ranging from 200-300 microstrains [34]. The resistance to moisture-induced damage was quantified by the Tensile Strength Ratio (TSR) according to AASHTO T 283 [35]. The fracture toughness or low-temperature cracking resistance was measured by the Semi-circular bend (SCB) test, wherein a load was incrementally applied on a notched half-disc sample at a rate of 0.5 mm/min based on ASTM D8044 [36] and AASHTO TP 124 [37]. The resultant load-line displacement (LLD) was monitored to calculate the critical strain energy release rate (J-integral, i.e., $J_c$).

Table 4 presents the mechanical test results of the coal-char bearing SMA mixture samples and the control group using 100% limestone aggregate. Even though there is a modest decline in the mechanical performance of the SMA mixture due to the addition of coal char aggregate, it still can fulfill the load-bearing demands. The shear strength of the coal-char bearing SMA sample was measured at 1.2 MPa, which lies within the range of 0.3 MPa - 1.5 MPa for commonly used surface dense-graded mixtures and open-graded

friction course mixtures [38,39]. The rutting depth of the coal-derived SMA sample was recorded as 3.72 mm under 50 °C after 8000 loading cycles. The electrically conductive SMA layer was primarily designed as the de-icing heating layer with minimal thickness. Thus, this thin layer will not compromise the overall rutting resistance of the entire pavement structure [40]. The tensile strength ratio (TSR), i.e., a metric for moisture susceptibility, was observed as 86.96% for the conductive SMA sample, indicating acceptable moisture resistance higher than the usual TSR failure limit of 80% [41]. The critical strain energy release rate ($J_c$) of the conductive SMA sample was calculated as 2.6 kJ/m$^2$, exhibiting its good resistance to low-temperature cracking. The mechanical test results demonstrate that coal char can serve as the main constituent of the conductive SMA mixture while ensuring pavement load-bearing performance.

Table 4 Mechanical Performance and sample sizes of SMA mixtures

| Material | Shear strength [MPa] | Rutting depth under 8000 cycles [mm] | TSR [%] | Resilient modulus [MPa] | $J_c$ [kJ/m$^2$] |
|---|---|---|---|---|---|
| Conductive SMA mixture (48.9 wt% coal char) | 1.2 | 3.72 | 86.96 | 490 | 2.6 |
| Control group (without coal char) | 2.43 | 1.71 | 92.85 | 2252 | 1.08 |
| Sample size | Shear test | Rutting resistance test | TSR test | Resilient modulus test | SCB test |
| Diameter (mm) | 100 | 150 | 100 | 150 | 150 |
| Thickness (mm) | 63.5 | 75 | 63.5 | 50 | 30 |

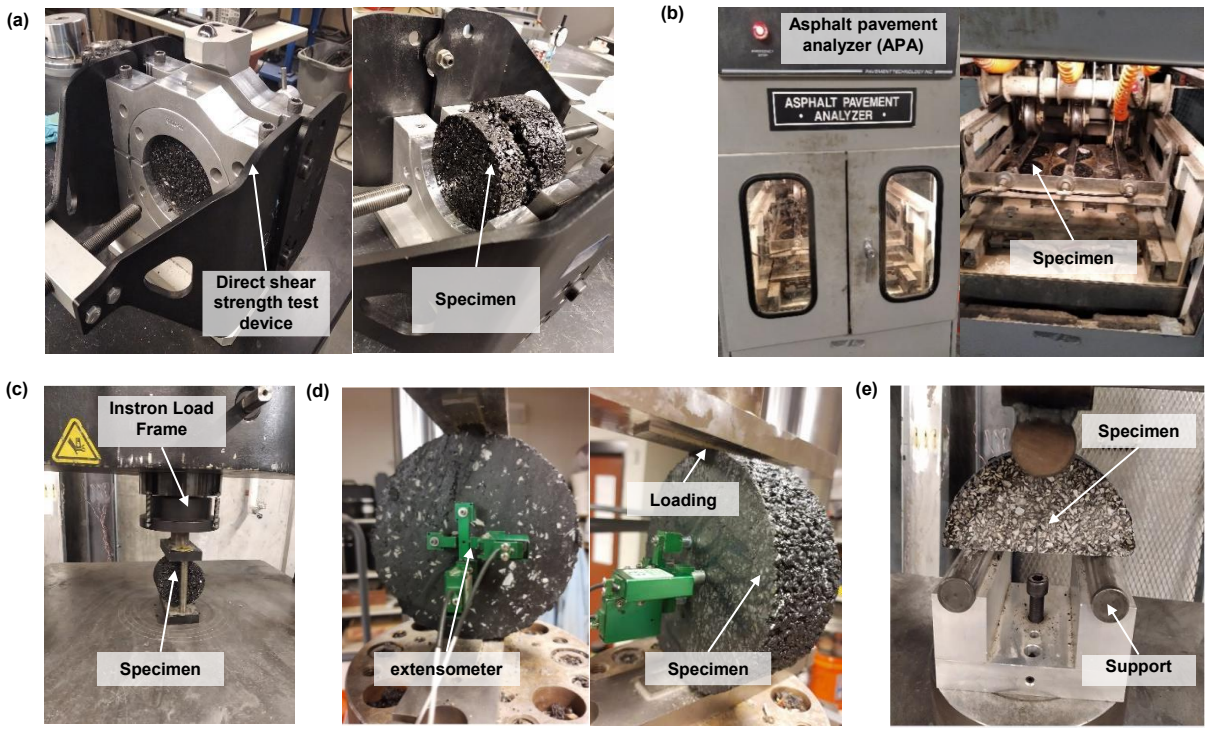


Figure 3 Mechanical test set-up: (a) direct shear test, (b) rutting susceptibility test using asphalt pavement analyzer (APA) test, (c) moisture susceptibility (TSR) test, (d) resilient modulus test, and (e) semi-circular bend (SCB) test.

*2.3.2. Electrical conductivity*

The electrical conductivity of the conductive SMA mixture was tested following the practice of standard ASTM C1876 [23] using *FLIR DM 62* Multimeter as shown in Figure 4 (a). During the test, two aluminum electrode plates were placed at both ends of the specimen with a diameter of 100 mm and a thickness of 76.2 mm. The electrical resistance ($R_E$) was measured under the incremental pressure from 0 to 900 kPa applied on the electrodes [42]. The volume resistivity ($\zeta$) is thereby calculated using Equation (1).

$$\zeta = R_E \frac{A_E}{L_E} \quad (1)$$

where $A_E$ (0.0081 $m^2$) is the cross-sectional area of the sample and $L_E$ (0.0762 m) is the distance between the two electrode plates. The electrical conductivity of the conductive

SMA sample, i.e., the inverse of the volume electrical resistivity, was measured corresponding to the applied pressure presented in Figure 4 (b). The results indicate that the electrical conductivity of the conductive SMA mixture increases approximately linearly with the incremental stress. Variable stress causes changes in contact area among the conductive coal char particles that dominate the overall electrical conductivity by forming an electrically conductive network within the material. As a result, this leads to the piezoresistive behavior of the material [42].

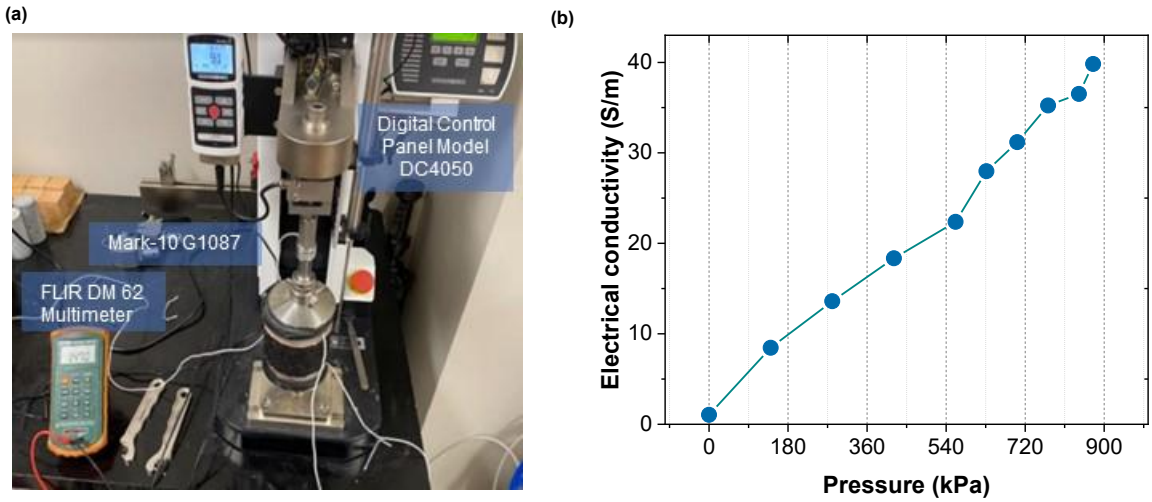


Figure 4 (a) Test setup to measure electrical resistance of the conductive SMA sample (b) Measured conductivity-pressure relationship of the conductive SMA sample

*2.3.3. Thermophysical properties*

As Figure 5 shows, the thermal conductivities of the asphalt mixtures were measured by a *HotDisk TPS1500* thermal constant analyzer following the transient plane source (TPS) method [26]. The thermal properties were obtained based on the recorded temperature changes of a plane source that heats the surrounding material to be measured. For this test, two identical samples were prepared with polished and washed surfaces. The specimens, with diameters of 100 mm and thicknesses of 50 mm, were kept under 110 ℃ for a 12-hour conditioning period in a convection oven before TPS testing. A

double-spirited nickel metal sensor supported by a 0.025-m Kapton was positioned between the two samples, see Figure 5 (b). This sensor functioned both as the heat source with a stepwise generation, and a monitor recording temperature variation simultaneously. Based on the time-variant heat captured by a high-impedance digital voltmeter, the thermal conductivity and thermal diffusivity were measured and computed through an iteration. The measured thermal properties of the asphalt mixture samples for the three pavement courses are presented in Table 5.

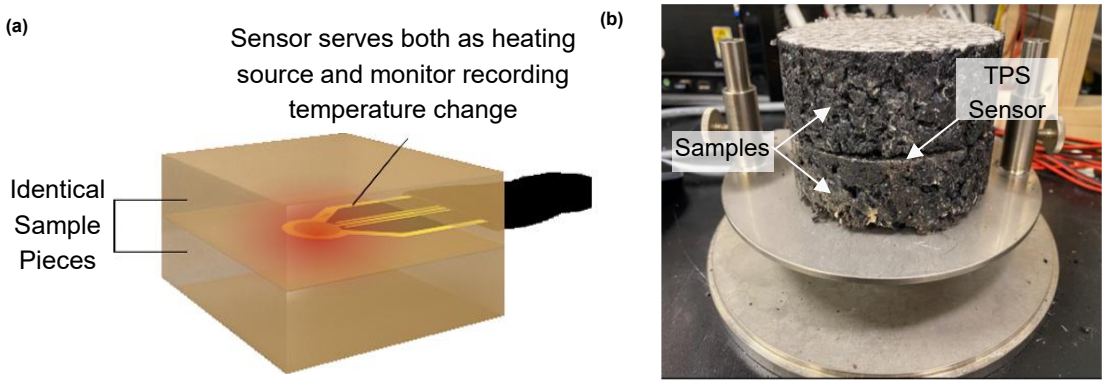


Figure 5 Transient plane source test to measure the thermal constants of materials: (a) illustrative figure; and (b) experimental setup for the asphalt mixture samples

Table 5 Material properties of the test samples

| Material layer | Density [kg/m$^3$] | Thermal conductivity[1] [W/(m·K)] | Specific heat[2] [J/(kg·K)] | Average solar absoptance[3] [–] |
|---|---|---|---|---|
| Surface course | 2361 | 2.23 | 591.23 | 0.666 |
| Conductive SMA mixture | 1445 | 1.06 | 741.00 | N.A. |
| Base course | 2401 | 2.07 | 622.40 | N.A. |

[1] Thermal conductivity was measured using the transient plane source (TPS) method according to ISO22007 specifications
[2] Specific heat was estimated using TPS method based on thermal diffusivity
[3] Solar absorptance was measured using a spectrophotometer with an integrating sphere

*2.3.4. Surface light reflectance*

The surface diffusive solar reflectance of the prototype pavement with dimensions of 16 inches (406.4 mm) in length, 13.5 inches (342.9 mm) in width, and 4 inches (101.6 mm) in thickness, was measured following the ASTM E903 specifications [43]. In this test, an ultraviolet-visible near-infrared (UV-VIS-NIR) spectrophotometer equipped with an integrating sphere attachment was employed. As indicated in Figure 6 (a), the spectrophotometer (*StellarNet Black Comet*) was used to capture the spectral characteristics of the test specimen within the wavelength range of approximately 300 nm to 1200 nm. A metal halide (MH) light source shown in Figure 6 (a) provided spectra within the 470-700 nm range. Throughout the experiment, the 100% line was measured by a high-reflectance reference specimen (barium sulfate), while the zero line was recorded in complete darkness. Figure 6 (b) presents the spectral reflectance of the prototype specimen surface at different wavelengths. The average absorptance $\bar{\alpha}$ of the prototype specimen surface is 66.6% over the measured spectrum.

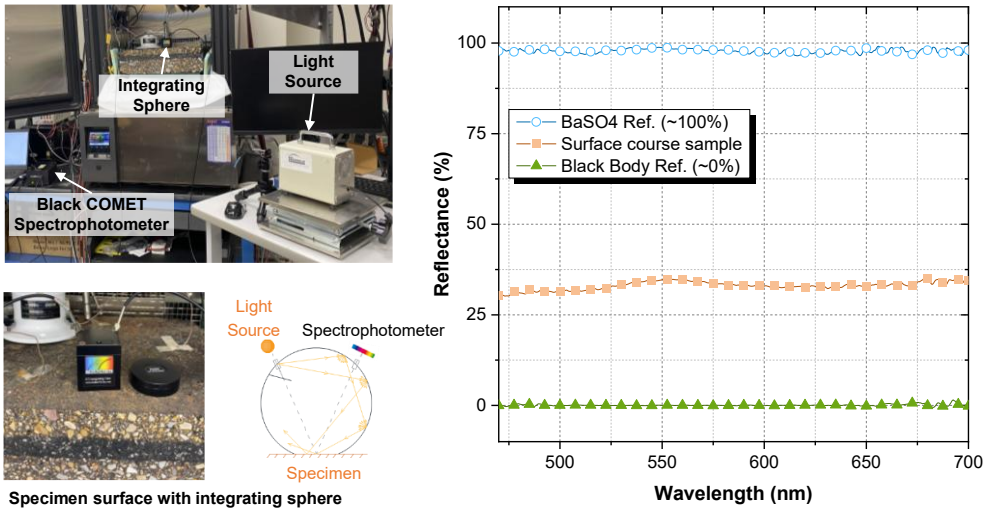


Figure 6 (a) Experimental setup to determine the light reflectance of the prototype specimen surface via the UV-VIS-NIR spectrophotometer and integrating sphere (b) Measured spectral reflectance of different specimens.

## 3. Bench-scale prototype testing and demonstration

### 3.1. Specimen preparation

To validate the feasibility of using coal-char bearing asphalt mixture for de-icing, a prototype pavement specimen was prepared using the materials designed in Section 2.1. As Figure 7 shows, a 16-inch (406.4 mm) × 16-inch (406.4 mm) × 4-inch (101.6 mm) slab was fabricated in the laboratory. Three different asphalt mixture layers were compacted within a wooden mold using a vibratory plate compactor, see Figure 7. The base course was compacted to a 2.25-inch thickness (57.15 mm), while the surface course was compacted to a thickness of 1-inch (25.4 mm). The middle layer, i.e., the conductive SMA mixture was compacted to 0.75 inches (19.05 mm). The target air void for each layer was designed as 7% under the field construction conditions. Due to the high asphalt content in the conductive SMA mixture, no tack coat was applied between adjacent asphalt layers. To embed electrodes into the prototype specimen for electric heating, two copper wire electrodes (110-H04) spaced 320 mm apart were embedded within the conductive SMA mixture, see Figure 7.

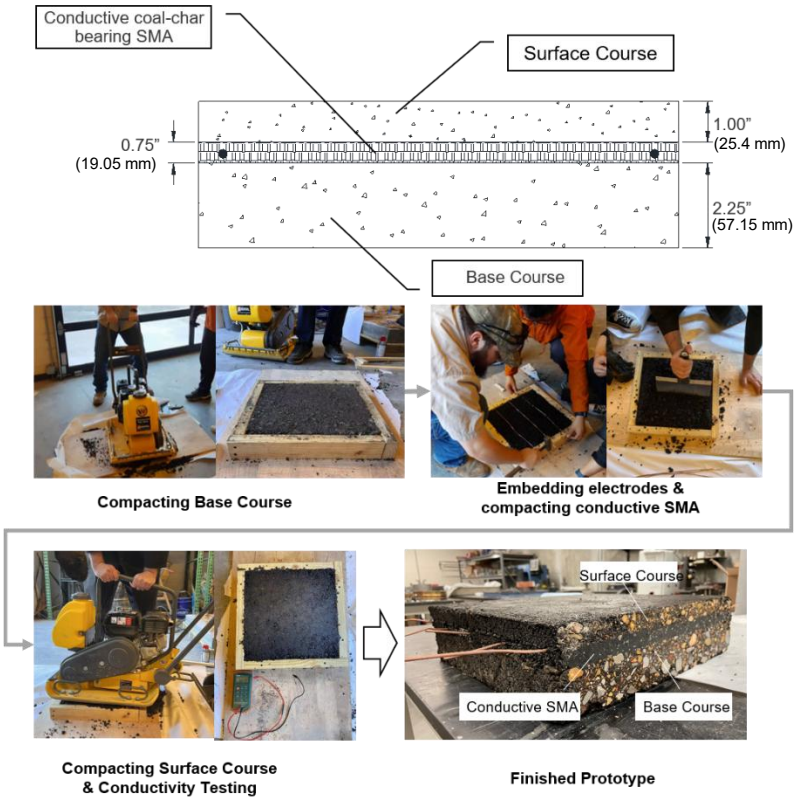


Figure 7 Test specimen preparation

### 3.2. Bench scale heated pavement test

#### *3.2.1. Test setup*

To study the de-icing performance of self-heating pavement, experiments were performed on the prototype specimen to analyze the thermal behavior of the conductive coal-char bearing SMA mixture with electric heating. As depicted in Figure 8, the 16-inch (406.4 mm) × 13.5-inch (342.9 mm) × 4-inch (101.6 mm) specimen and test apparatus were placed in an environmental chamber (*ESPEC Inc.*). This environmental chamber controlled ambient temperature and relative humidity (RH) using an RTD air temperature sensor and a solid-state relative humidity (RH) sensor during the tests. The prototype specimen was tested in two scenarios, i.e., the specimen with electric heating

without radiation and the unheated one under radiation, see Figure 8 (a) and (b). The tests were conducted under 1-D heat transfer conditions by encasing the specimen in an insulated box. The top and bottom surface temperature changes were monitored by multiple thermocouple sensors mounted on the prototype specimen, as illustrated by a schematic and photos shown in Figure 8. In addition, aluminum foil domes were employed to shield the temperature sensors from direct irradiation heat. Data were collected at 2-second intervals by a *National Instrument PXI-express* data acquisition system. To study the impacts of solar and atmospheric radiation, a 450-watt MH lamp was fixed on customized stands facing the prototype specimen in the environmental chamber. The visible light, along with partial ultraviolet and infrared radiation was measured using a pyranometer (*Eppley Laboratory, Inc.*). The conductive SMA layer was charged by a direct current (DC) power source via two embedded copper wire electrodes, where the voltage and current output were monitored continuously. During these experiments, the test conditions were maintained with the measured air temperature at around -5°C, the measured relative humidity (RH) at around 10% to 15%, and the incident irradiance at around 500 $W/m^2$ on the specimen surface.

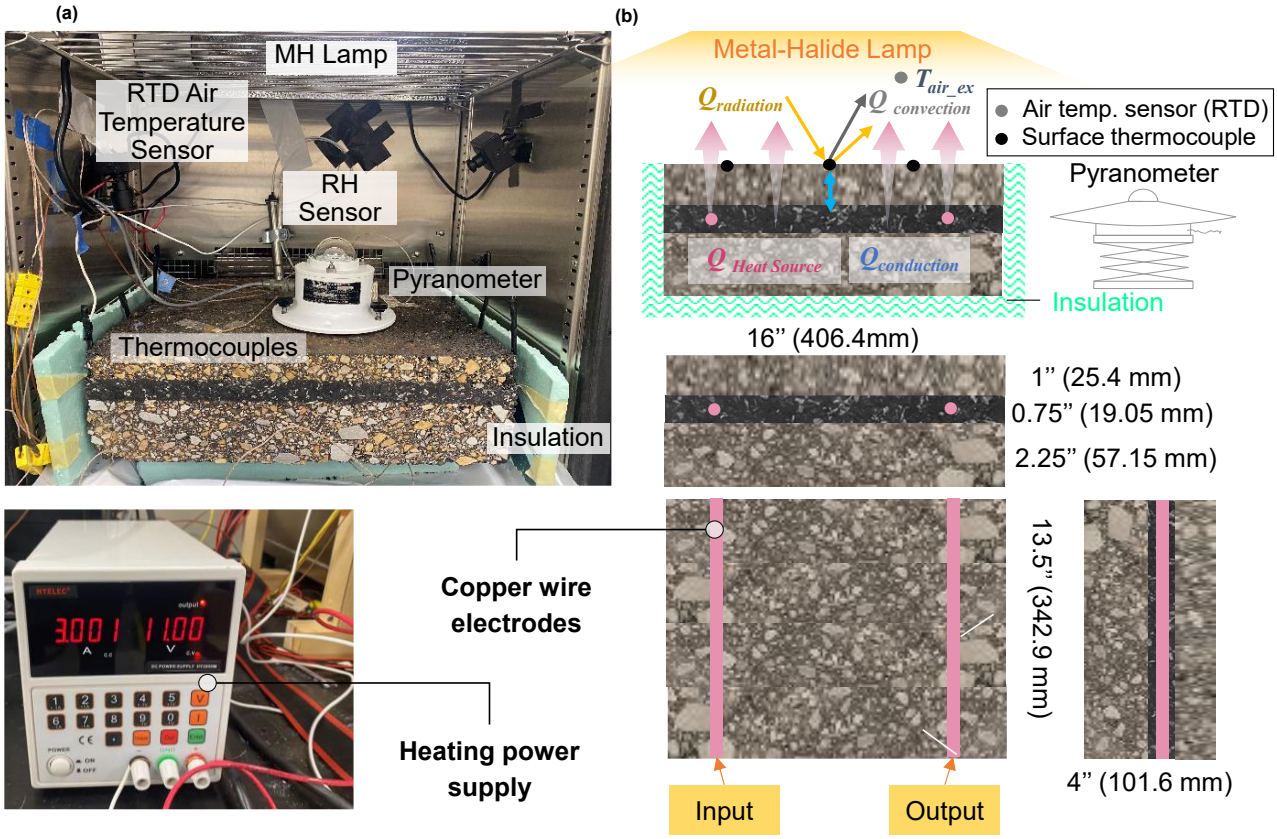


Figure 8 Experimental setup and instrumentation: (a) setup to test the thermal behavior of self-heating pavement prototype specimen; (b) schematic for instrumentation

*3.2.2. Test result*

The experimental investigations in the thermal behavior of the pavement de-icing system using Ohmic heating were conducted in two scenarios: 1) the heated specimen without radiation and 2) the unheated specimen under radiation. In the heating test, the specimen was initially conditioned in the environmental chamber, followed by activating heating power until surface temperatures reached a steady state. The experimental results under heating mode are presented in Figure 9 (a) and (b). When the prototype specimen's top surface temperature became stable, the heater was turned off and the MH lamp was activated with the results during a representative period presented in Figure 9 (c) and (d).

The measured heating power output of the electric de-icing system was controlled at around 30 W (215 W/m$^2$) during the first test.

As shown in Figure 9 (a) and (b), the top surface temperature of the prototype specimen gradually increased by 2.5℃ during the first 100 minutes and stabilized at 5℃. This indicates the effectiveness of the electrically conductive SMA heating layer as a heating layer for de-icing. Figures 9 (c) and (d) present the thermal behavior of the prototype specimen under radiation to study the impact of solar radiation. The measured temperature profiles indicate that the top surface temperature of the prototype specimen was effectively maintained over 15℃ under radiation. The de-icing system only needs to be triggered under precipitation with outdoor air temperature below 0℃. The surface temperature profiles of the prototype specimen were also used to calibrate the thermal network model developed in the following section for simulation analysis in Section 5.

It is noted that since a small bench-scale prototype was tested here, the electrical resistance between the two electrodes was measured only at 9.82 ohms. This largely restricted the heating power output as the laboratory DC power supply was limited to 3A in consideration of safety.

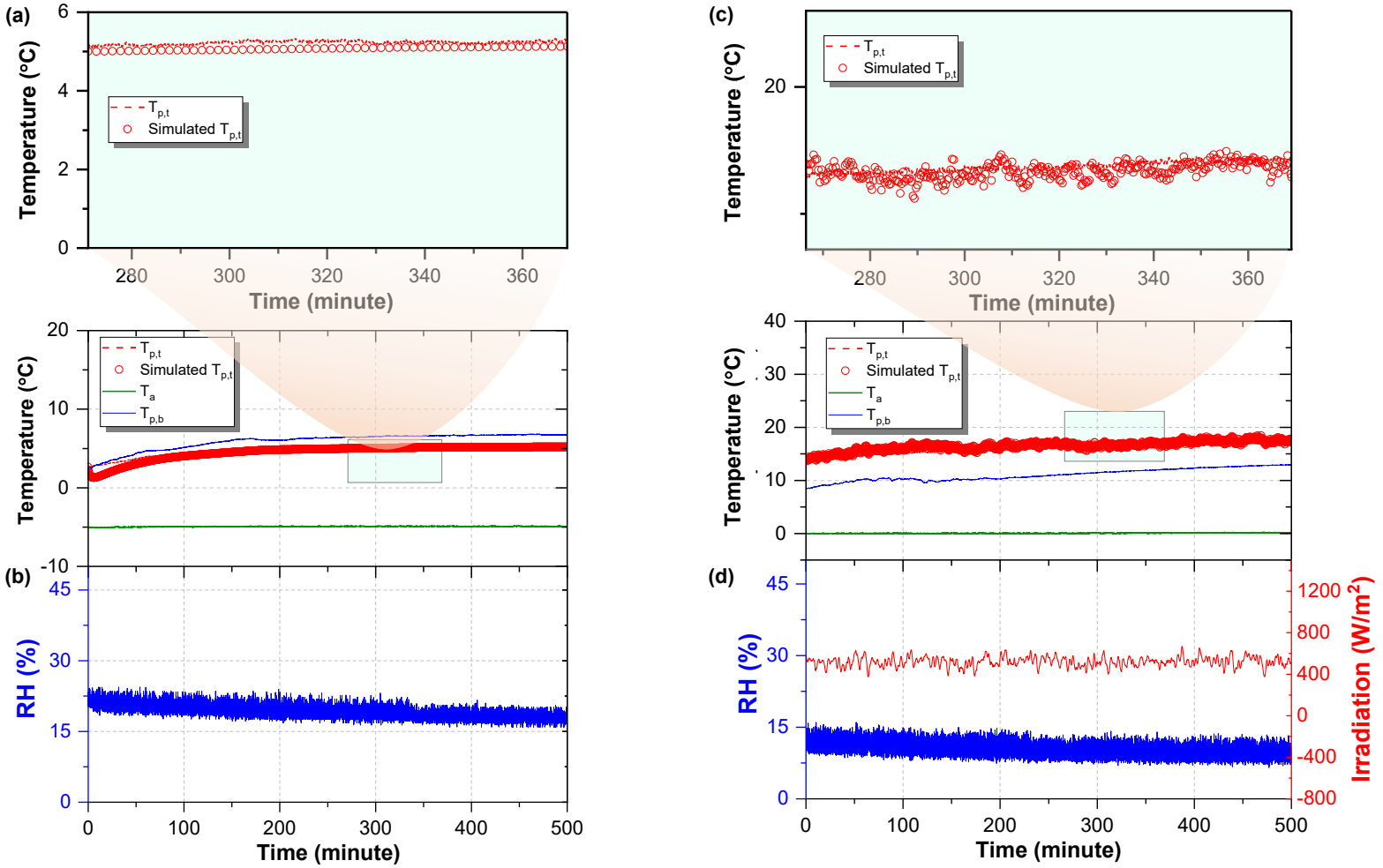


Figure 9 Measured and simulated temperature profiles of heated prototype specimen: (a) tested and simulated temperature of the top surface, tested bottom surface temperature and environmental chamber air temperature; (b) measured relative humidity; and measured and simulated temperature of unheated prototype specimen under radiation: (c) tested and simulated temperature of the top surface, tested bottom surface temperature and environmental chamber air temperature; (d) measured relative humidity and irradiation

Following the calibration tests, a de-icing experiment was conducted in the environmental chamber with crushed ice packed on top of the prototype pavement specimen as shown in Figure 10. The de-icing experiment was carried out in an environmental chamber (*ESPEC Inc.*) with its internal air temperature set at -10℃ and RH set at 15%. The heating power supply was configured to 12V to provide a heating flow of 50 - 60W (358.3 - 430 W/$m^2$) through the prototype pavement panel. It was observed that the crushed ice melted within 120-150 minutes after activating the heating power supply, as presented in Figure 10 (a). The temperature profiles of the prototype cross section soon after the test started and the top surface temperature after the prototype specimen reached a steady state were captured by thermal images shown in Figure 10 (b). The thermal images indicate that the temperature of the conductive SMA heating layer was higher than the adjacent layers by over 8℃ and the surface course temperature quickly exceeded 0℃ during the early stage of the test. This demonstrates the effective de-icing performance of this electrically conductive coal-char bearing SMA mixture. Furthermore, it highlights the potential of this coal-derived asphalt mixture for commercial applications in pavement de-icing systems to improve winter roadway maintenance. The construction of this conductive pavement substitutes normal aggregates with coal char particles, allowing the use of existing equipment and machinery from current road construction practices to lower barriers for scale-up applications.

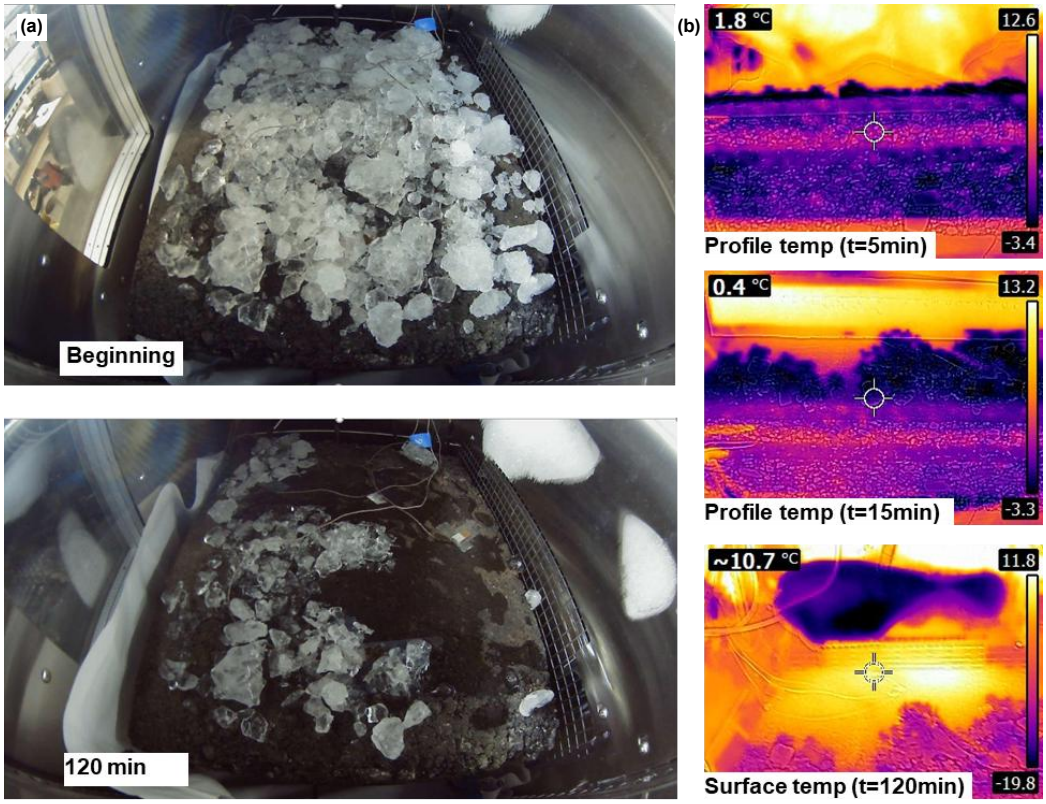


Figure 10 (a) De-icing experiment of the prototype pavement specimen; (b) Temperature profiles of the prototype cross section and top surface recorded by infrared thermal camera during the test

## 4. Modeling and simulation of the self-heating pavement

### 4.1. Heat transfer model formulation

To predict the transient thermal behavior of the self-heating pavement in various scenarios, a thermal network model based on a finite difference approach [44] was developed. The 1-D heat transfer equation for any point with temperature $T$ within the asphalt mixture material can be expressed as:

$$\rho c_p \frac{\partial T}{\partial t} = \lambda \frac{\partial}{\partial x}\left(\frac{\partial T}{\partial x}\right) + q_v(t) \tag{2}$$

where $t$ is time; $c_p$, $\rho$, and $\lambda$ are the material's specific heat, density, and thermal conductivity, respectively; and $q_v$ is the rate of heat generated (or dissipated) within the

material (e.g., electric heating).

For a differential control volume, Equation (2) is expressed as:

$$\int_V \rho c_p \frac{\partial T}{\partial t} dV = \int_V \left[ \lambda \frac{\partial}{\partial x}\left( \frac{\partial T}{\partial x} \right) \right] dV + \dot{E}_V \tag{3}$$

where $V$ is volume and $\dot{E}_V$ is the rate of heat transferred from energy sources/sinks in this differential control volume.

Each material layer of the pavement can be discretized into a number of finite volumes represented by a nodal network as shown in Figure 11. Thus, Equation (2) can be rewritten as a general form for node $i$ in a thermal network as:

$$\int_{V_i} c_{p,i} \rho_i dV_i \frac{\partial T_i}{\partial t} = H_i^{i-1} T_{i-1} + H_i^{i+1} T_{i+1} - \left( H_i^{i-1} + H_i^{i+1} \right) T_i + Q_i \tag{4}$$

where the subscript $i$ represents the node number; $H_i^{i-1}$ is the heat transfer coefficient representing conduction between node $i$-1 and node $i$; $Q_i$ is the rate of heat transfer from energy sources in the finite volume of node $i$.

The heat balance at the exterior surface node $i$ of the pavement considers effects due to convective heat exchange, heat conduction, short-wave radiation, $Q_{i,sw}$, and long-wave radiation, $Q_{i,lw,}$ with outdoor environments and internal material,_which can be expressed as:

$$\int_{V_i} c_{p,i}\rho_i dV_i \frac{\partial T_i}{\partial t} = H_i^{air_ex}\left(T_{air_ex} - T_{i,}\right) + H_i^{i-1}T_{i-1} + H_i^{i+1}T_{i+1} - \left(H_i^{i-1} + H_i^{i+1}\right)T_i + Q_{i,sw} + Q_{i,lw} \tag{5-a}$$

$$Q_{i,sw} = \bar{\alpha}_i I_s^{\downarrow} A_i \tag{5-b}$$

$$Q_{i,lw} = \left[F_i^{sky}\left(T_{sky,abs}^4 - T_{i,abs}^4\right) + F_i^{grd}\left(T_{grd,abs}^4 - T_{i,abs}^4\right) + F_i^{air_ex}\left(T_{air_ex,abs}^4 - T_{i,abs}^4\right)\right] \cdot \sigma\varepsilon_i A_i + \sum_k \sigma\varepsilon_i F_i^k \left(T_{k,abs}^4 - T_{i,abs}^4\right)A_k \tag{5-c}$$

where $\bar{\alpha}_i$ is solar absorptance; $F_i^k$ is view factor for node $i$ with exterior emitting surface $k$ – i.e., emitting surfaces; $\sigma$ is Stephan-Boltzmann constant.

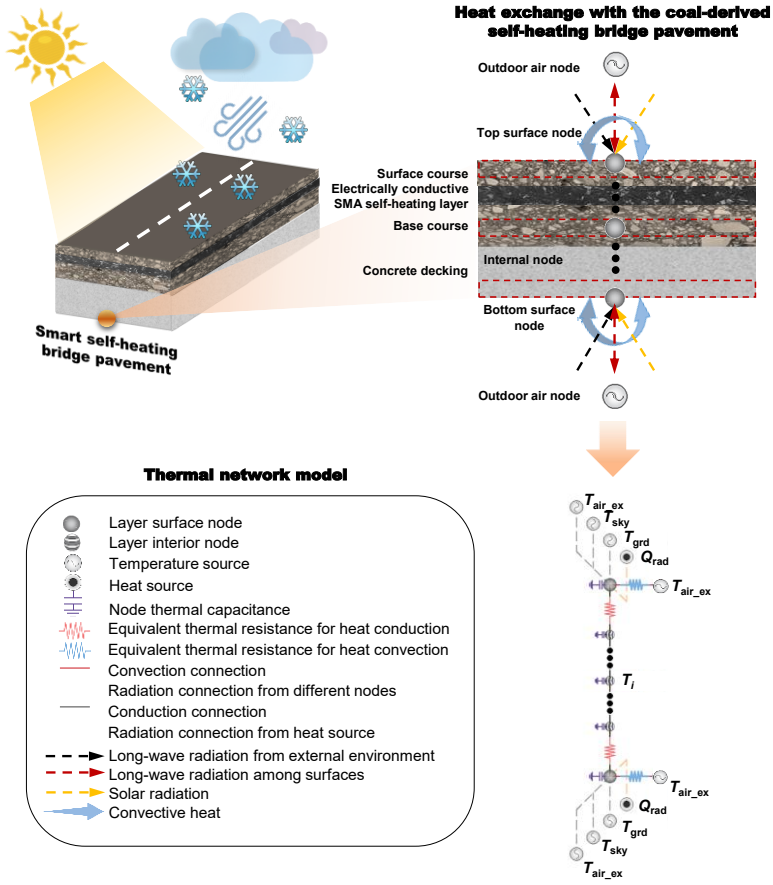


Figure 11 Thermal network model of self-heating bridge pavement with an electric de-icing system

For internal nodes (non-surface nodes) within the self-heating layer of the smart pavement with an electric de-icing system, the heat balance is written as:

$$\int_{V_i} c_{p,i}\rho_i dV_i \frac{\partial T_i}{\partial t} = H_i^{i-1}T_{i-1} + H_i^{i+1}T_{i+1} - \left(H_i^{i-1} + H_i^{i+1}\right)T_i + Q_{i,el} \quad (6)$$

Where $Q_{i,el}$ is the heat rate generated by the electric de-icing system.

For internal nodes within the normal pavements without electric heating, only heat conduction takes place with the following heat balance:

$$\int_{V_i} c_{p,i}\rho_i dV_i \frac{\partial T_i}{\partial t} = H_i^{i-1}T_{i-1} + H_i^{i+1}T_{i+1} - \left(H_i^{i-1} + H_i^{i+1}\right)T_i \quad (7)$$

The thermal network was assembled using the same methodology developed in the authors' previous work with high computational efficiency [27,45]. More details of numerical computation can be found in the prior study of the authors [27,45].

### 4.2. Model validation

The model was calibrated by comparing the simulated temperature profiles with the experimental results presented in Section 3.2. The experiment was regarded as a 1-D heat transfer process given that all surfaces of the specimens excluding the top surface were considered as adiabatic via direct contact with insulation panels. Accordingly, the measured specimen bottom surface temperature $T_{p,b}$ served as the boundary condition in the simulation of the experimental conditions. Ideal thermal contact between layers was assumed, thus interface resistance was negligible. As a result, long-wave radiation was deemed negligible in the experimental setup. Consequently, the term $Q_{i,lw}$ can be neglected in Equation (4-a) for the heat balance of the exterior surface node. The heat balance of the specimen top surface exposed to the controlled environmental chamber is

determined by ambient air temperature $T_{air_ex}$, and irradiation intensity $I_s^{\downarrow}$ measured by the pyranometer based on the equations outlined in Section 4.1.

Figures 9 (a) - (b) present comparisons between the simulated top surface temperature $T_{p,t}$ of the specimen under electric heating without radiation and the experimental data. While simulated top surface temperature $T_{p,t}$ of the specimen without electric heating under radiation is shown in Figure 9 (c) - (d) as compared to the experimental results. The agreement between temperature profiles in different scenarios indicated the satisfactory performance of the thermal network model.

## 5. Case study

### 5.1. Simulation details

To evaluate the potential of the coal-derived smart self-heating pavement in scale-up field applications, simulation case studies were performed on a bridge pavement under different climate conditions. The thermal performance of the pavement and energy consumption of the de-icing system using electric heating were analyzed, see Figure 12. The analysis was conducted on a single lane of a bridge measuring 30 feet (9.14 m) in length, 12 feet (3.66 m) in width, and 12.5 inches (0.32 m) in thickness. The pavement configuration consists of a coal-char charged SMA layer sandwiched between the asphalt surface course and base course and on top of 6-inch-thick concrete decking, as shown in Figure 12. The coal-char bearing SMA layer functions as a heating element for de-icing. The de-icing system with embedded electrodes was covered by a waterproof film with negligible thermal resistance. This design guarantees heating performance while preventing water penetration.

In the case study, the measured material properties including density, thermal conductivity, specific heat, and solar absorptance presented in Section 2 (Table 5). Whole-year heat transfer and energy simulations were performed using the calibrated thermal nwtowrk model in MATLAB for the bridge pavements located in areas susceptible to weather-related car crashes. Typical meteorological year 3 (TMY3) weather data were utilized to analyze the thermal behavior and electricity cost of the self-heating bridge pavements in three representative cities, i.e., Pittsburgh, Pennsylvania (ASHRAE climate zone 5A, cool humid), Minneapolis, Minnesota (ASHRAE climate zone 6A, cold humid), and Fairbanks, Alaska (ASHRAE climate zone 8, subarctic/arctic), respectively.

Moreover, a simple control strategy was designed for the electric heating de-icing system. The proposed control rule for the heating power of the pavement de-icing system with adaptive output voltage is presented in Figure 13. In this control implementation, the control system is mainly composed of a sensor to measure the top surface temperature $T_{p,t}$ of the pavement, a central automation controller, and one adjustable voltage regulator. According to the test results of the self-heating de-icing system in section 3.2, the electric heating system is turned on when there is precipitation (snow or rain) applied on the pavement ( $L_{\text{pre}} > 0$ ) with the top surface temperature $T_{p,t}$ under 0℃. The output heating power $P_{out}$ of the electric heating de-icing system applied on the bridge pavement is quantified by Equation (8):

$$P_{out} = \varphi_{el} P_{\max} \tag{8-a}$$

$$\varphi_{el} = \varphi_0 + (1 - \varphi_0) \frac{C_1 - T_{p,t}}{C_2} \tag{8-b}$$

where $P_{\max}$ is the maximum output of the electric heating de-icing system, which is prescribed as 500W/m$^2$, 700W/m$^2$, and 1000W/m$^2$ for the scenarios in Pittsburgh, Minneapolis, and Fairbanks in the case study, respectively; $\varphi_0$ , $C_1$ and $C_2$ are constants.

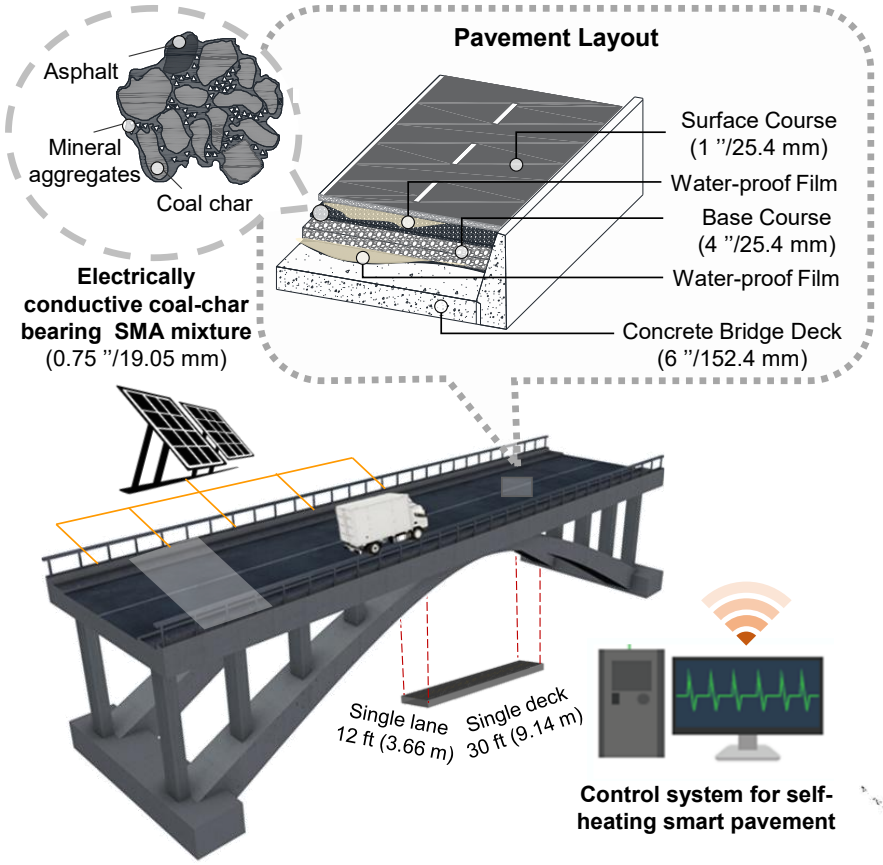


**Whole-year transient heat transfer simulations**

❖ Typical meteorological year 3 (TMY3) weather data

- Pittsburgh, Pennsylvania (ASHRAE climate zone 5A, cool humid)
- Minneapolis, Minnesota (ASHRAE climate zone 6A cold humid)
- Fairbanks, Alaska (ASHRAE climate zone 8, subarctic/arctic)

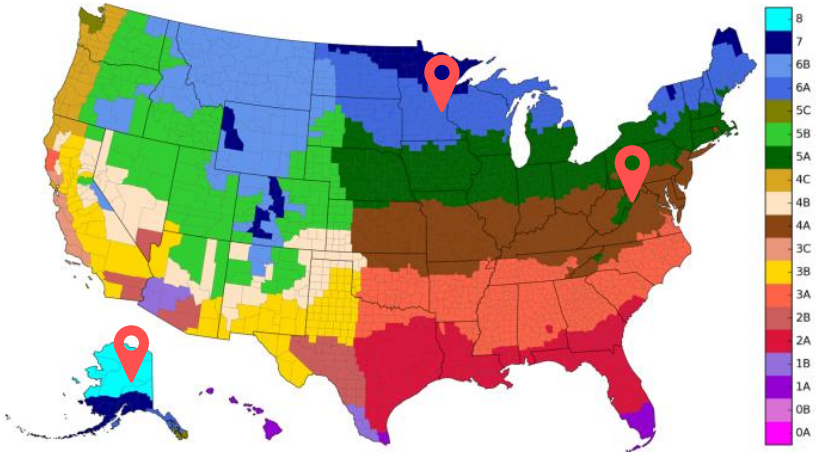


Figure 12 Simulation case study details

The response of the voltage regulator is triggered by the pavement's top surface temperature $T_{p,t}$. When the pavement's top surface temperature is below zero under precipitation, the output voltage is determined by:

$$U_{out} = U_{mag}\sqrt{\min(\varphi_{el},1)} \tag{9}$$

where $U_{out}$ is the output voltage; $U_{mag}$ is the magnitude of the voltage power supply.

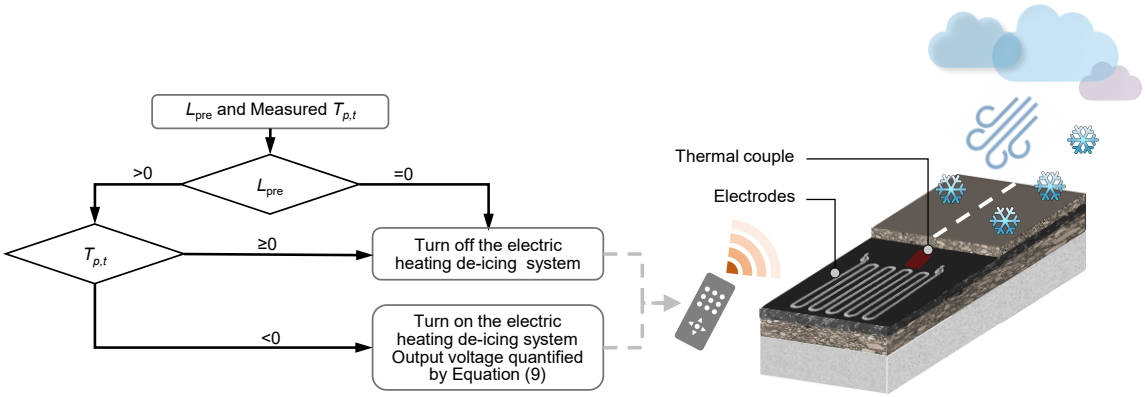


Figure 13 Control rule for the electric heating de-icing system of the smart self-heating pavement

## 5.2. Results and discussion

### *5.2.1. Thermal behavior*

The weather conditions, the heating power output of the de-icing system, and surface temperature profiles of self-heating pavement and the baseline are presented in Figure 14 - Figure 16. The comparisons between these two cases during a representative winter week in Pittsburgh (cool humid climate zone), Minneapolis (cold humid climate zone), and Fairbanks (subarctic/arctic climate zone) are presented.

Figure 14 (a) illustrates the thermal behavior of the self-heating bridge pavement equipped with the electric de-icing system in comparison with the baseline pavement

(without electric heating) in January in Pittsburg. The outdoor air temperatures fluctuated between -6 ℃ to 10 ℃ with relatively high solar radiation as shown in Figure 14 (b). Both the baseline and the self-heating pavement top surface temperatures were close and mostly over zero when the outdoor environment was relatively warm without precipitation, see the time histories plotted in Figure 14 (a) and (b). However, during the early morning of January 20$^{th}$, the outdoor air temperature fell below 0℃ under the impact of the snow event with low solar radiation as presented in Figure 14 (b). Accordingly, the top surface temperature of the baseline pavement gradually decreased to -2 ℃. In contrast, the de-icing system of the self-heating pavement was triggered when its top surface temperature approached the freezing point as shown in Figure 14 (a). Therefore, the top surface temperature was effectively maintained over 0℃ under snowfall (shadowed in a light green area) from January 20$^{th}$ to January 21$^{st}$ during cold mornings and nights. On January 22$^{nd}$, under rising outdoor environment temperatures without precipitation, the electric heating de-icing system was automatically turned off. Consequently, the pavement top surface temperature of the two cases gradually converged again. As Figure 14 (c) shows, the heating power output of the electric de-icing system fluctuated around 350 W/m$^2$ during snowy days. The de-icing system's heating power output stayed below its maximum (500W/m$^2$) and the top surface temperature remained slightly over 0℃ under milder environmental conditions. This demonstrated the efficiency of the controller.

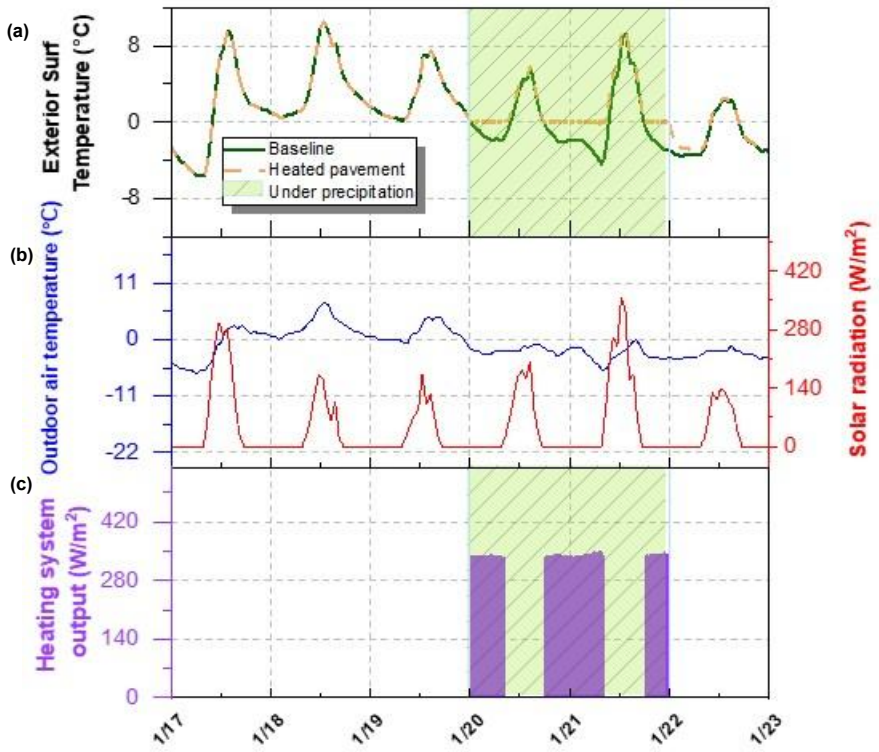


Figure 14 Thermal behavior of the self-heating pavement with electric de-icing system during representative winter days in Pittsburgh: (a) comparison of top surface temperature between baseline and the self-heating pavement with electric de-icing system (b) outdoor air temperature and solar radiation (c) output of the electric heating de-icing system

Figures 15 (a) - (c) show significantly colder outdoor environment with more frequent snow events in January in Minneapolis as compared to the scenario in Pittsburg. Figure 15 (b) presents the outdoor air temperature predominantly below zero with a range within -14 ℃ - 2 ℃ under moderate solar radiation over the representative winter week. As a result, the top surface temperature of the baseline pavement varied between -26 ℃ to -7 ℃ under extreme weather conditions as presented in Figure 15 (a). Whereas the self-heating pavement was consistently maintained above freezing by the electric de-icing system throughout this period, see Figure 15 (a). Despite the continuous snowfall as shaded in a light green area in Figure 15 (a), the electric heater was not continuously active throughout the whole winter month shown in Figure 15 (c). For instance, on

January 17th, the top surface temperature of the self-heating pavement exceeded zero under rising solar radiation during the daytime. This led to the deactivation of the electric de-icing system to fully leverage the solar heat gains, see Figure 15 (a). Subsequently, the electric heating de-icing system remained inactive during the daytime or night under warmer weather conditions. It is observed that the peak heating power output of the electric de-icing system in January in Minneapolis fluctuated between 240 W/m$^2$ to 540 W/m$^2$ in Figure 15 (c). The heating power output determined by the varied weather-induced demands was much lower than the magnitude designated at 700W/m$^2$.

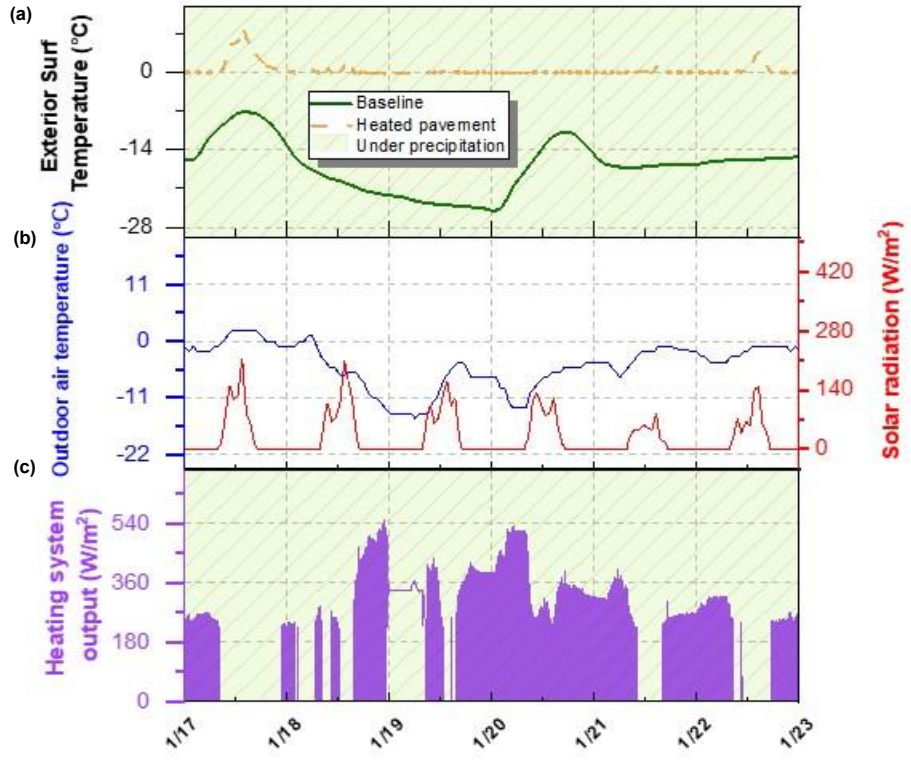


Figure 15 Thermal behavior of the self-heating pavement with electric de-icing system during representative winter days in Minneapolis: (a) comparison of top surface temperature between baseline and the self-heating pavement with electric de-icing system (b) outdoor air temperature and solar radiation (c) output of the electric heating de-icing system

The thermal behavior of the baseline and self-heating pavements, along with de-icing system output and weather conditions during a representative week in January in Fairbanks are plotted in Figure 16. The severe weather conditions under cold spells are presented in Figure 16 (b), with outdoor air temperature ranging from -22℃ to -2℃ throughout this period. The peak solar radiation only reached up to 35 W/m$^2$ while the snow events occupied the whole winter week, see Figure 16 (b) and (c). Consequently, the top surface temperature of the baseline pavement exposed to weather extremes remained far below zero with variations between -17 ℃ to -2 ℃ as presented in Figure 15 (a). In contrast, the electric de-icing system of the self-heating pavement was frequently activated as presented in Figure 15 (c). Similar to the prior two scenarios, its top surface temperature was maintained close to zero throughout the cold winter, see Figure 15 (a). The peak output of the electric de-icing system during January in Fairbanks fluctuated between 750 W/m$^2$ and 925 W/m$^2$ under exposure to extremely cold weather conditions in Figure 15 (c). This heating power output was close to the designed magnitude of 1000W/m$^2$ and thereby it took notably higher energy costs than scenarios in Pittsburgh and Minneapolis.

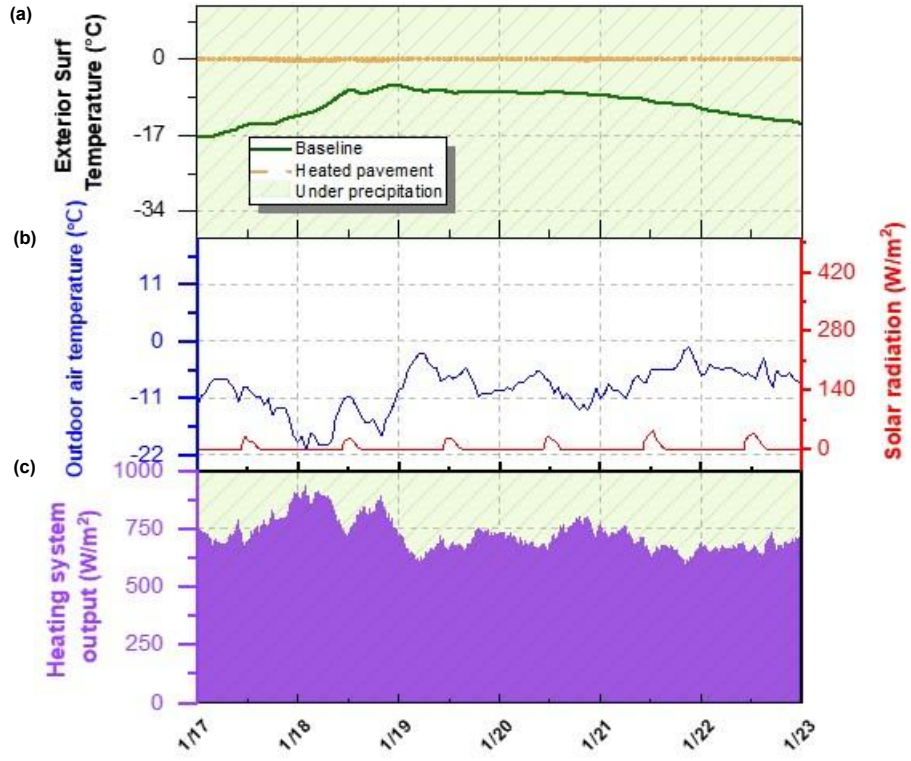


Figure 16 Thermal behavior of the self-heating pavement with electric de-icing system during representative winter days in Fairbanks: (a) comparison of top surface temperature between baseline and the self-heating pavement with electric de-icing system (b) outdoor air temperature and solar radiation (c) output of the electric heating de-icing system

*5.2.2. Energy consumption of the pavement de-icing system*

Figure 17 presents the simulated monthly energy consumption per unit area of the electric de-icing system in Pittsburgh (cool humid climate zone), Minneapolis (cold humid climate zone), and Fairbanks (subarctic/arctic climate zone), respectively. For the smart self-heating pavement located in cool humid climate zones such as Pittsburgh, the electric de-icing system was only activated in cold and humid winter months under snow impacts. Therefore, the monthly energy consumptions associated with low precipitation were lower than 5 kWh/m$^2$ in December and January under cold environments, see Figure 17 (a). Under deteriorated weather conditions in cold humid climate zones (e.g.,

Minneapolis) and subarctic/arctic climate zones (e.g., Fairbanks), the operational period of the electric de-icing system for the self-heating pavement extended beyond winter months to cold transitional seasons. For instance, the electric de-icing system in Minneapolis consumed 7.2 kWh/$m^2$ in November and 53.3 kWh/$m^2$ in March for heating as shown in Figure 17 (b). While the energy consumption in Fairbanks was recorded at 151.7 kWh/$m^2$, 28.4 kWh/$m^2$, 70.3 kWh/$m^2$, and 300.4 kWh/$m^2$ in March, April, October, and November, respectively.

Consequently, the monthly energy consumption augmented under extreme weather conditions. The maximum monthly energy consumption of the electric de-icing system incrementally reached 16.2 kWh/$m^2$, 172.9 kWh/$m^{2,}$ and 343.4 kWh/$m^2$ in Minneapolis and Fairbanks, respectively. Similarly, the annual energy consumption of the self-heating pavement exhibits the same trend with 24.6 kWh/$m^2$, 457.4 kWh/$m^{2,}$ and 1444.8 kWh/$m^2$ in Pittsburgh, Minneapolis, and Fairbanks, respectively.

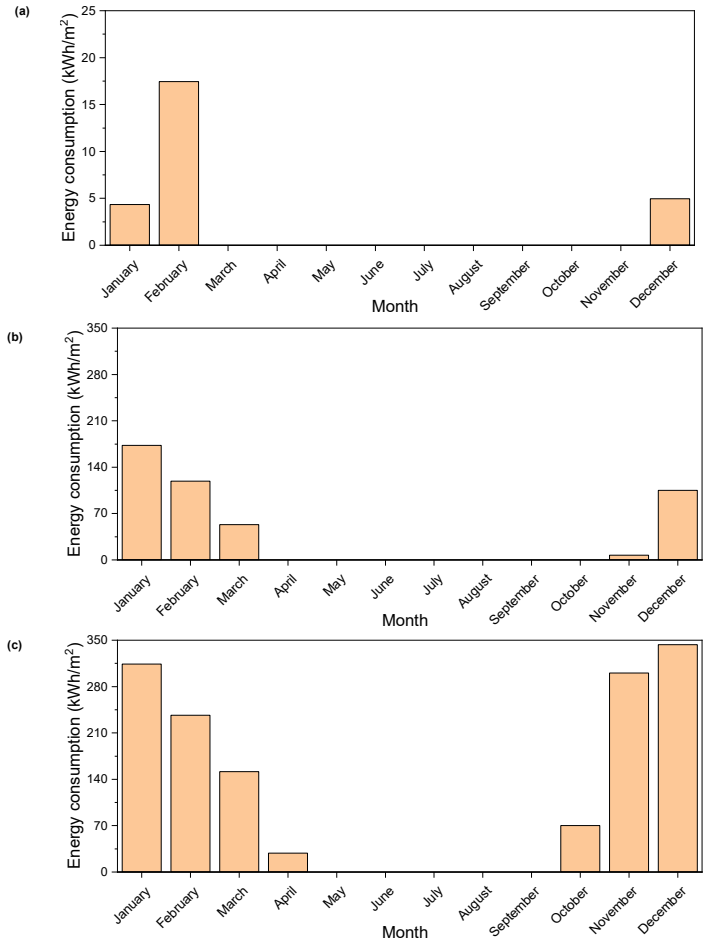


Figure 17 Monthly energy consumption of the electric de-icing system in (a) Pittsburgh (b) Minneapolis and (c) Fairbanks

## 6. Conclusions

In this research, a novel low-cost coal-char bearing multifunctional asphalt pavement material was developed and demonstrated for smart self-heating pavements. An innovative pathway to designing and constructing a self-heating pavement system was proposed through incorporating the byproduct of coal pyrolysis, i.e., coal char, into the pavement structure to build an embedded de-icing system. This coal-derived carbon exhibits tunable electrical conductivity, higher cost-efficiency, and wider compatibility for aggregate alternatives compared with other conductive pavement additives. Furthermore, the application of coal char in multifunctional pavements reduces the traditional utilization as fuels by direct burning, which mitigates negative impacts on the built and natural environment. The self-heating pavement was designed and manufactured according to TDOT specification, SMA mixture design standard by NAPA, and Superpave mix design manual. It consists of the coal-char charged Stone Mastic Asphalt (SMA) mixture sandwiched between two non-conductive asphalt mixtures. The mechanical, electrical, and thermophysical properties of the innovative electrically conductive coal-char bearing pavement material were comprehensively characterized through multiscale material tests. To assess the thermal behavior and de-icing performance of this coal-char charged conductive asphalt pavement, bench-scale slab heating and de-icing tests were conducted on a laboratory prototype. To study the transient thermal behavior of the heating pavement, a thermal network model with high computational efficiency was developed and experimentally calibrated. Simulation case studies were performed on a full-scale bridge pavement to evaluate its potential in field applications. The main findings and contributions of this research are summarized below:

- Coal chars have similar shapes and sizes to those of regular aggregates or fillers adopted in pavements, they can serve either as coarse aggregates or fine fillers smaller than 75μm for asphalt mastics. Accordingly, the construction of coal-char bearing pavements partially replace normal aggregates with coal char particles. This wider compatibility for aggregate alternatives enables the seamless extension to low-cost commercialization.
- Microstructural analysis (i.e., X-ray micro-computed tomography and scanning electron microscopy) indicates that the coal-char acts as the primary constitute to formulate the electrically conductive network and contact force chains for load bearing as the matrix. Consequently, the mechanical and electrical properties of the conductive SMA mixture are predominantly governed by the interactions among the coal-char particles, which are significantly affected by the applied stress. The mechanical tests of the conductive SMA mixture with coal char aggregate demonstrated acceptable performance as load-bearing materials and showed satisfactory stiffness, fracture toughness to low-temperature cracking, moisture resistance, and rutting resistance. The electrical conductivity variation range of the conductive SMA mixture is significantly higher than existing conductive pavement material alternatives for the electric heating de-icing system. The satisfactory thermophysical properties of the conductive SMA mixture ensure efficient heat conduction for de-icing.
- The bench-scale slab heating and de-icing experiments showcased the de-icing performance of the prototype. The coal-char bearing SMA can serve as

an effective de-icing system to enhance pavement resilience against climate impacts. The thermal network model was validated using the experimental results obtained from the bench-scale slab heating test of the prototype.

- Simulation case studies were performed on a bridge pavement in Pittsburgh, Minneapolis, and Fairbanks across cool humid, cold humid, and subarctic/arctic climate zones. The thermal behavior of the heating pavement was analyzed using the thermal network model. The whole-year transient heat transfer simulation results indicate that the self-heating pavement surface temperature was effectively maintained above zero under cold weather conditions with precipitation. The annual energy consumption of this pavement de-icing system was 24.6 $kWh/m^2$, 457.4 $kWh/m^{2,}$ and 1444.8 $kWh/m^2$ in Pittsburgh, Minneapolis, and Fairbanks, respectively. The simulation results indicated the promise for future field applications.

Further studies are needed to quantify the environmental benefits and economic viability of this new pavement system for filed applications.

## Conflict of Interests

The authors declare no conflict-of-interests.


## Acknowledgments

This research was made possible by the U.S. Department of Energy (DOE) Office of Fossil Energy (DE-FE0031983). The funding support from DOE and National Energy Technology Laboratory (NETL) is greatly appreciated.

## Reference List


[1] U.S Department of Transport. Federal Highway Adminastration. How Do Weather Events Impact Roads? Online 2015. https://ops.fhwa.dot.gov/weather/q1_roadimpact.htm#:~:text=Weather acts through visibility impairments,traffic flow%2C and agency productivity.

[2] Qiu L, Nixon WA. Effects of adverse weather on traffic crashes: Systematic review and meta-analysis. Transp Res Rec 2008:139–46. https://doi.org/10.3141/2055-16.

[3] Lépy É, Rantala S, Huusko A, Nieminen P, Hippi M, Rautio A. Role of winter weather conditions and slipperiness on tourists' accidents in Finland. Int J Environ Res Public Health 2016;13. https://doi.org/10.3390/ijerph13080822.

[4] Yi X, Chen L, Yu W, Guo M, Chen L. State of the art and practice of pavement anti-icing and de-icing techniques Sciences in Cold and Arid Regions State of the art and practice of pavement anti-icing and de-icing techniques. Sci Cold Arid Reg 2014;6:14–21. https://doi.org/10.37
24/SP.J.1226.2014.00014.State.

[5] Chen J, Ma X, Wang H, Xie P, Huang W. Experimental study on anti-icing and deicing performance of polyurethane concrete as road surface layer. Constr Build Mater 2018;161:598–605. https://doi.org/10.1016/j.conbuildmat.2017.11.170.

[6] Fay L, Akin M, Shi X, Veneziano D. Winter Operations and Salt , Sand and Chemical Management , of the Final Report on NCHRP. vol. 25. 2013.

[7] Henderson DJ. Experimental roadway heating project on a bridge approach. Highw Res Rec 1965;111:14–25.

[8] Rew Y, Shi X, Choi K, Park P. Structural Design and Lifecycle Assessment of Heated Pavement Using Conductive Asphalt. J Infrastruct Syst 2018;24. https://doi.org/10.1061/(asce)is.1943-555x.0000440.

[9] Rew Y, Baranikumar A, Tamashausky A V, El-Tawil S, Park P. Electrical and mechanical properties of asphaltic composites containing carbon based fillers. Constr Build Mater 2017;135:394–404. https://doi.org/10.1016/j.conbuildmat.2016.12.221.

[10] Wu S, Pan P, Chen M, Zhang Y. Analysis of Characteristics of Electrically Conductive Asphalt Concrete Prepared by Multiplex Conductive Materials. J Mater Civ Eng 2013;25:871–9. https://doi.org/10.1061/(asce)mt.1943-5533.0000565.

[11] Gopalakrishnan K, Ceylan H, Kim S, Yang S, Abdualla H. Electrically conductive mortar characterization for self-heating airfield concrete pavement mix design. Int J Pavement Res Technol 2015;8:315–24. https://doi.org/10.6135/ijprt.org.tw/2015.8(5).315.

[12] Chung DDL. Electrically conductive cement-based materials. Adv Cem Res 2004;16:167–76. https://doi.org/10.1680/adcr.16.4.167.46658.

[13] Zhao H, Wu Z, Wang S, Zheng J, Che G. Concrete pavement deicing with carbon fiber heating wires. Cold Reg Sci Technol 2011;65:413–20. https://doi.org/10.1016/j.coldregions.2010.10.010.

[14] Yu X, Hurley MT, Li T, Lei G, Pedarla A, Puppala AJ. Experimental feasibility study of a new attached hydronic loop design for geothermal heating of bridge decks. Appl Therm Eng 2020;164:114507. https://doi.org/10.1016/j.applthermaleng.2019.114507.

[15] Sassani A, Ceylan H, Kim S, Arabzadeh A, Taylor PC. Development of Carbon Fiber-modi fi ed Electrically Conductive Concrete for Implementation in Des Moines International Airport. Case Stud Constr Mater 2018;8:277–91. https://doi.org/10.1016/j.cscm.2018.02.003.

[16] Minsk LD. Electrically conductive asphalt for control of snow and ice accumulation. Highw Res Rec 1968;227:57–63.

[17] Ahmedzade P, Sengoz B. Evaluation of steel slag coarse aggregate in hot mix asphalt concrete. J Hazard Mater 2009;165:300–5. https://doi.org/10.1016/j.jhazmat.2008.09.105.

[18] Pan P, Wu S, Xiao F, Pang L, Xiao Y. Conductive asphalt concrete: A review on structure design, performance, and practical applications. J Intell Mater Syst Struct 2015;26:755–69. https://doi.org/10.1177/1045389X14530594.

[19] Notani MA, Arabzadeh A, Ceylan H, Kim S, Gopalakrishnan K. Effect of Carbon-Fiber Properties on Volumetrics and Ohmic Heating of Electrically Conductive Asphalt Concrete. J Mater Civ Eng 2019;31:04019200. https://doi.org/10.1061/(asce)mt.1943-5533.0002868.

[20] Wu S, Mo L, Shui Z, Chen Z. Investigation of the conductivity of asphalt concrete containing conductive fillers. Carbon N Y 2005;43:1358–63. https://doi.org/10.1016/j.carbon.2004.12.033.

[21] Slebi-Acevedo CJ, Lastra-González P, Pascual-Muñoz P, Castro-Fresno D. Mechanical performance of fibers in hot mix asphalt: A review. Constr Build Mater 2019;200:756–69. https://doi.org/10.1016/j.conbuildmat.2018.12.171.

[22] Liu X, Wu S. Study on the graphite and carbon fiber modified asphalt concrete. Constr Build Mater 2011;25:1807–11. https://doi.org/10.1016/j.conbuildmat.2010.11.082.

[23] Biswas K, Shukla Y, Desjarlais A, Rawal R. Thermal characterization of full-scale PCM products and numerical simulations, including hysteresis, to evaluate energy impacts in an envelope application. Appl Therm Eng 2018;138:501–12. https://doi.org/10.1016/j.applthermaleng.2018.04.090.

[24] Liu X, Nie Z, Wu S, Wang C. Self-monitoring application of conductive asphalt concrete under indirect tensile deformation. Case Stud Constr Mater 2015;3:70–7. https://doi.org/10.1016/j.cscm.2015.07.002.

[25] American Association of State Highway and Transportation Officials. AASHTO T 340

Standard Method of Test for Determining Rutting Susceptibility of Hot Mix Asphalt (HMA) Using the Asphalt Pavement Analyzer (APA). American Association of State Highway and Transportation Officials (AASHTO); 2023.

[26] International Organization for Standardization. ISO 22007-2 Plastics Determination of thermal conductivity and thermal diffusivity Part 2: Transient plane heat source (hot disc) method. International Organization for Standardization; 2022.

[27] He Y, Zhou H, Fahimi F. Modeling and demand-based control of responsive building envelope with integrated thermal mass and active thermal insulations. Energy Build 2022;276:112495. https://doi.org/10.1016/j.enbuild.2022.112495.

[28] Tennessee DOT. Tennessee DOT Standard Specifications for Road and Bridge 2021.

[29] NAPA NAPA. SMA Guideline QIS122- Designing and constructing SMA Mixtures 2002:99.

[30] Hube GA, Kennedy TW, Anderson M. The Superpave Mix Design Manual for New Construction and Overlays. 2010.

[31] Liu S, Liu H, Liu H, Xia Z, Zhao Y, Zhai J. Numerical simulation of mesomechanical properties of limestone containing dissolved hole and persistent joint. Theor Appl Fract Mech 2022;122:103572. https://doi.org/10.1016/j.tafmec.2022.103572.

[32] Jackson GS, Sanders E. Research Performance Progress Report (RPPR) | grants.nih.gov 2019:1–26.

[33] Song W, Shu X, Huang B, Woods M. Influence of Interface Characteristics on the Shear Performance between Open-Graded Friction Course and Underlying Layer. J Mater Civ Eng 2017;29:1–9. https://doi.org/10.1061/(asce)mt.1943-5533.0001907.

[34] Roque R, Buttlar WG. Development of a measurement and analysis system to accurately determine asphalt concrete properties using the indirect tensile mode. Asph Paving Technol Assoc Asph Paving Technol Tech Sess 1992;61:304–32.

[35] American association of state highway and transportation Officials. AASHTO T 283 Standard method of test for resistance of compacted asphalt mixtures to moisture-induced damage. 2022nd ed. American Association of State Highway and Transportation Officials (AASHTO); 2022.

[36] American Society for Testing and Materials International. ASTM D8044 Standard Test Method for Evaluation of Asphalt Mixture Cracking Resistance using the Semi-Circular Bend Test (SCB) at Intermediate Temperatures. American Society for Testing and Materials International; 2016. https://doi.org/10.1520/D8044-16.Copyright.

[37] American Association of State Highway and Transportation Officials. AASHTO TP 124 Standard Method of Test for Determining the Fracture Potential of Asphalt Mixtures Using the Illinois Flexibility Index Test (I-FIT). American Association of State Highway and Transportation Officials (AASHTO); 2020.

[38] Song W, Ph D, Shu X, Ph D, Asce AM, Huang B, et al. Effects of Asphalt Mixture Type on Asphalt Pavement Interlayer Shear Properties 2018;4:1–7. https://doi.org/10.1061/JPEODX.0000056.

[39] Song W, Shu X, Huang B, Woods M. Factors affecting shear strength between open-graded friction course and underlying layer. Constr Build Mater 2015;101:527–35. https://doi.org/10.1016/j.conbuildmat.2015.10.036.

[40] Wang Y, Chen X, Lu H, Xiao R, Hu W, Jiang X, et al. Laboratory investigation on electrical and mechanical properties of asphalt mixtures for potential snow-melting and deicing pavements. Constr Build Mater 2024;413:134901. https://doi.org/10.1016/j.conbuildmat.2024.134901.

[41] Cooley J, Brown ER. Potential o
f using stone matrix asphalt for thin overlays. Transp Res Rec 2001:46–52. https://doi.org/10.3141/1749-07.

[42] woo Jeon W, Ryu B, Choo H. Effect of applied vertical stress on the electrical conductivity of particulate mixtures containing both electrically conductive and nonconductive particles: experimental study on recovered carbon black. Granul Matter 2022;24:1–10. https://doi.org/10.1007/s10035-021-01170-x.

[43] Performance M, Spectrophotom- NI, Mass A, Solar Z, Tables I, Materials S, et al. Standard Test Method for Solar Absorptance , Reflectance , and Transmittance of Materials Using Integrating Spheres 1 1996;03:1–9. https://doi.org/10.1520/E0903-20.2.

[44] Theodore L. Bergman, Frank P. Incropera, David P. DeWitt ASL. Fundamentals of heat and mass transfer. Seventh Ed. John Wiley & Sons, Inc.; 2011.

[45] He Y, Zhang Y, Zhang C, Zhou H. Energy-saving potential of 3D printed concrete building with integrated living wall. Energy Build 2020;222:110110. https://doi.org/10.1016/j.enbuild.2020.110110.